Vortex-induced vibrations of three staggered circular cylinders at low Reynolds numbers

Suresh Behara, B. Ravikanth, and Venu Chandra

Citation: Physics of Fluids **29**, 083606 (2017); doi: 10.1063/1.4998417
View online: http://dx.doi.org/10.1063/1.4998417
View Table of Contents: http://aip.scitation.org/toc/phf/29/8
Published by the American Institute of Physics

Vortex-induced vibrations of three staggered circular cylinders at low Reynolds numbers

Suresh Behara,[1,2,a)] B. Ravikanth,[2] and Venu Chandra[3]
[1]*Department of Mechanical Engineering, Aditya Institute of Technology and Management, Tekkali, AP 532201, India*
[2]*ESI Software (I) Pvt. Ltd., 27th Cross, Banashankari 2nd Stage, Bangalore, KA 560070, India*
[3]*Department of Civil Engineering, Indian Institute of Technology Madras, Chennai, TN 600036, India*

(Received 27 January 2017; accepted 20 July 2017; published online 16 August 2017)

Vortex-induced vibrations of three staggered circular cylinders are investigated via two-dimensional finite element computations. All the cylinders are of equal diameter (D) and are mounted on elastic supports in both streamwise ($x-$) and transverse ($y-$) directions. The two downstream cylinders are placed symmetrically on either side of the upstream body at a streamwise gap of $5D$, with the vertical distance between them being $3D$. Flow simulations are carried out for Reynolds numbers (Re) in the range of Re = 60-160. Reduced mass (m^*) of 10 is considered and the damping is set to zero value. The present investigations show that the upstream cylinder exhibits initial and lower synchronization response modes like an isolated cylinder does at low Re. Whereas for both the downstream cylinders, the upper lock-in branch also appears. The initial and the upper modes are characterized by periodic oscillations, while the lower lock-in branch is associated with nonperiodic vibrations. The 2S mode of vortex shedding is observed in the near wake of all the cylinders for all Re, except for the upper branch corresponding to the downstream bodies. In the upper branch, both the downstream cylinders shed the primary vortices of the P+S mode. For the upstream cylinder, the phase between lift and the transverse displacement exhibits a 180° jump at certain Re in the lower branch. On the other hand, the downstream bodies undergo transverse oscillations in phase with lift in all lock-in modes, while the phase jumps by 180° as the oscillation response reaches the desynchronization regime. *Published by AIP Publishing.* [http://dx.doi.org/10.1063/1.4998417]

I. INTRODUCTION

Vortex-induced vibration (VIV) of multiple cylinders is a generic phenomenon of fluid-structure interaction (FSI), which provides several complex physical aspects yet to be understood, and has high practical significance in various engineering fields. Cylinder to cylinder interaction in the flow leads to completely different vibration responses exhibited by the bodies, compared with that of an isolated cylinder. Earlier research in understanding the dynamic behaviour of multiple cylinders is compiled in the review articles presented by Zdravkovich,[1,2] Chen,[3] and Sumner.[4] It is well known that as the vibration frequency (f_v) of an isolated cylinder mounted on elastic supports and the frequency of primary vortex shedding (f) lock-in with the natural frequency (f_N) of the spring-mass system, the body exhibits various synchronized oscillation response modes.[5] However, in the case of multiple cylinders, a few studies[6–21] showed that the downstream cylinders, due to the wake interference, do not exhibit distinct lock-in response modes or never experience synchronization at all. In order to further understand the VIV of circular cylinders that are subject to interaction with the wake of a freely oscillating cylinder, we herein present the numerical investigations of three cylinders arranged in staggered configuration. In the rest of the paper, various nondimensional parameters shall be mentioned, which are defined as follows: Reynolds number $(Re) = \rho UD/\mu$; Strouhal number $(St) = fD/U$; reduced velocity $(U^*) = U/(f_N D)$; reduced mass $(m^*) = 4m/(\pi\rho D^2)$; reduced natural frequency $(F_N) = 1/U^*$. Here, ρ, μ, and m represent density, dynamic viscosity of the fluid, and cylinder mass, respectively. D is the cylinder diameter.

Hover and Triantafyllou,[8] in laboratory experiments of two cylinders arranged in tandem and staggered configurations for $Re = 3 \times 10^4$, observed only galloping repose of the downstream cylinder, where the amplitude increases monotonically with the increase in reduced velocity. They did not notice resonance in their experiments for the oscillating downstream cylinder that is placed in the wake of stationary upstream one. Assi *et al.*[9] also observed galloping response of the downstream cylinder, as it vibrates in the wake of a static upstream body, for $3000 \le Re \le 13\,000$. Bokaian and Geoola[6] reported that for $Re \sim 10^3 - 5 \times 10^4$, the downstream cylinder, which freely oscillates in the wake of a fixed cylinder, exhibits synchronization or galloping response depending upon the gap between the cylinders. Brika and Laneville[7] carried out experimental studies of a long flexible cylinder placed in the wake of a stationary identical cylinder in tandem and staggered arrangements. They observed that the downstream cylinder, for a gap of $7D$–$8.5D$ between the two cylinders, exhibits galloping response. With increase in the gap up to $25D$, Brika and Laneville[7] found that the downstream body undergoes

a)sureshbehara@adityatekkali.edu.in

synchronized oscillations. However, in their studies, the amplitude response is described as a single and continuous curve, without the presence of the upper and the lower modes, which can be seen for an isolated cylinder.[22]

In order to further understand the effect of the gap between the cylinders on the dynamic response of the downstream bodies, Assi *et al.*[23] studied the wake-induced vibrations of two tandem cylinders, which are placed with a streamwise gap of 4D–20D. They observed that for small gaps considered in their experiments, due to the wake interference, the downstream cylinder undergoes synchronized oscillations at certain values of U^*. However, beyond this synchronization regime, the downstream body exhibits galloping-like response, where the maximum oscillation amplitude increases monotonically with an increase in U^*. Whereas for large gaps, as the influence of wake interference decreases, the downstream cylinder behaves like an isolated vibrating cylinder. Mittal and Kumar,[24] in the computations of two cylinders placed in tandem and staggered arrangements at Re = 100, observed soft lock-in, where the cylinders oscillate at a frequency, slightly less than the natural frequency of the system. Papaioannou *et al.*,[10] via numerical simulations of two tandem vibrating cylinders in the Re = 160 flow, demonstrated that along with the upstream cylinder, the downstream one also undergoes lock-in oscillations for the gap of 5D and smaller. In their studies, the amplitude response first increases with the increase in reduced velocity and then decreases as U^* is further increased, without exhibiting distinct synchronization response modes. In the computational investigations of two oscillating cylinders, placed in tandem and staggered arrangements with the streamwise gap of 5.5D, Prasanth and Mittal[11] observed that the downstream cylinder exhibits higher amplitude oscillations compared with the vibration behavior of the upstream body, at Re = 100. However, they did not perform sufficient analysis of the lock-in regime.

In contrast to the oscillation behavior of the multiple cylinder system, the dynamic response of an isolated cylinder is always associated with different lock-in modes. In the laboratory experiments of an isolated cylinder, conducted by Brika and Laneville,[25] it is observed that the synchronization regime is characterized by the initial and the lower response modes, for Re = 3400 – 11 800. Brika and Laneville[25] also noticed the upper response branch as the flow velocity is increased in small steps. However, this upper branch is not realized when the flow velocity is decreased from the lower branch. Therefore, one can argue that the upper branch is not stable in their studies. On the other hand, Prasanth and Mittal,[26] via numerical simulations for Re < 200, showed that the single cylinder exhibits only initial and lower lock-in branches. Khalak and Williamson,[22] and Govardhan and Williamson[27] demonstrated that for an isolated cylinder, which can vibrate in the transverse direction only, the upper response mode appears in addition to the initial and lower branches at $Re \sim O(10^4)$. However, Khalak and Williamson[22] noticed that the upper branch is associated with nonperiodic vibrations, while the lower branch is characterized by periodic oscillations. They attributed the reason for the appearance of the stable upper branch to the low mass-damping ($m^*\xi$) employed in their experiments.

Williamson and Roshko[28] demonstrated that for Re = 500 – 1000, the high amplitude response of an oscillating cylinder in the synchronization regime affects the wake pattern, by changing the timing of vortex shedding. They suggested that depending on the number of vortices released from the body for one oscillating cycle, shedding patterns can be categorized into 2S, 2P, and P+S modes. In the 2S mode, two single vortices of the opposite sign are shed for one shedding cycle, while two pairs are released in the 2P pattern. Whereas in the asymmetric mode of P+S, for each cycle, one pair of opposite vortices and a single vortex are shed. In the numerical simulations of two cylinders at Re = 160, Papaioannou *et al.*[10] found only the 2S shedding mode for all the U^* considered. Brika and Laneville[7] observed that the downstream cylinder in the wake of a stationary cylinder sheds the 2S mode of vortices for all the flow velocities before the resonance occurs, while after resonance the wake is associated with the 2P shedding pattern. At low Re (<200), Prasanth and Mittal[26] observed only the 2S mode for both initial and lower lock-in regimes in the case of an isolated cylinder. Whereas Khalak and Williamson[22] and Govardhan and Williamson[27] showed that the wake of a single cylinder is characterized by the 2S shedding pattern in the initial response branch and changes to the 2P mode as the oscillation response jumps to the upper branch. They further noticed that the 2P mode persists even in the lower lock-in branch. Blackburn and Henderson,[29] in the computations of the Re = 250 flow past a freely vibrating cylinder, observed only the 2S mode. They argued that the 2P mode is not necessarily associated with the large amplitude plateau in the lock-in regime.

Williamson in a private communication, as referred to by Blackburn and Henderson,[29] showed the P+S mode, obtained in the wake of a single cylinder that undergoes forced transverse oscillations with peak amplitude of 0.6D at Re = 140. Blackburn and Henderson[29] also observed the P+S mode in the wake of a forced oscillating cylinder with high transverse amplitude for Re = 250, in their two-dimensional computations. As the amplitude is decreased to 0.75D, they noticed that the P+S mode still persists. On the other hand, Singh and Mittal,[30] via two-dimensional numerical simulations showed that the P+S mode occurs in the wake of an oscillating cylinder at Re = 350. Note that Blackburn and Henderson,[29] and Singh and Mittal[30] carried out 2D simulations for $Re \geq 250$, where the flow is fully three-dimensional. In the present 2D computations of three freely oscillating staggered cylinders for $Re \leq 160$, where the flow is two-dimensional, we observed that the downstream cylinders shed the P+S mode of vortices in one of the synchronization regimes for $102 \leq Re \leq 124$, with the peak amplitude being above 0.9D. Interestingly, Han *et al.*[20] observed the P+S mode, shed by the downstream cylinder that is placed in tandem in the wake of a stationary cylinder at Re = 160, even as the body vibrates at low amplitudes corresponding to the nonsynchronization regime.

Prasanth and Mittal[26] reported that the phase between the lift and the transverse displacement of isolated cylinder jumps from nearly 0° to 180° at a Reynolds number in the lower branch, where f_v/f_N crosses 1.0. In their experimental studies, Brika and Laneville[7] observed for a single cylinder

that the jump in the amplitude response from the initial to the lower response branch is associated with a 180° jump in phase. Also, they noticed that this jump in the amplitude response is hysteretic. On the other hand, Khalak and Williamson[22] and Govardhan and Williamson[27] showed that a single cylinder experiences a sudden jump in the amplitude from the initial to the upper branch, and this transition is associated with hysteresis. On the other hand, the upper ⇒ lower mode transition is characterized by mode switching, and therefore there is no hysteresis. However, Khalak and Williamson[22] observed a 180° phase jump in the transition from the upper to the lower branch. In the case of two cylinders, Brika and Laneville[7] reported that the jumps in the amplitude response as well as hysteresis are completely absent in the dynamic response of the downstream cylinder. In the present paper, we shall show that the downstream cylinders exhibit a gradual transition from the initial to the upper lock-in branch, while a jump occurs in the amplitude response at the upper ⇒ lower branch transition. Also, hysteresis is observed in this transition. We shall further show that the 180° phase jump occurs at different *Re* for the upstream and the two downstream cylinders.

To summarize the discussion of the effect of the streamwise gap on the dynamic response of downstream cylinders, for the gaps less than 4*D*, vortex shedding from the upstream cylinder does not occur. Therefore, the downstream cylinder vibrates along with the oscillating upstream one. It is observed in several previous studies that as the primary vortices are shed by the upstream body in the gap (greater than 4*D*), the downstream cylinder exhibits galloping response due to its interaction with the upstream vortices. However, the lock-in regime corresponding to the downstream cylinders is not clearly understood. In the present work, with an objective of studying the lock-in regime of the downstream cylinders, we studied the vortex-induced vibrations of three freely oscillating circular cylinders arranged in staggered configuration with the streamwise distance of 5*D* between the upstream and both the downstream cylinders, and lateral distance of 3*D* between the two downstream bodies. All the cylinders are identical and are mounted on elastic supports in both the *x*- and *y*-directions. Reduced mass (m^*) of 10 and zero damping ($\xi = 0$) are considered for all the simulations. We observed that the Strouhal frequency in the wake of stationary cylinders at $Re = 100$ is 0.156. Therefore, specifying the normalized natural frequency, $F_N = 0.156$ at $Re = 100$ as design condition, stabilized space-time finite element computations are carried out for $60 \leq Re \leq 160$ in two dimensions. *Re* is gradually increased by providing the flow corresponding to the previous *Re* as the initial condition.

II. GOVERNING EQUATIONS AND FINITE ELEMENT FORMULATION

A. The Navier-Stokes equations

Assume that $\Omega_t \subset \mathbb{R}^{n_{sd}}$ and $(0, T)$ are the spatial and temporal domains, respectively, where n_{sd} is the number of space dimensions. Let Γ_t represent the boundary of Ω_t, while $\mathbf{x}$ and t denote the spatial and temporal coordinates, respectively. The Navier-Stokes equations governing incompressible Newtonian fluid flow are

$$\rho\left(\frac{\partial \mathbf{u}}{\partial t} + \mathbf{u}\cdot\nabla\mathbf{u} - \mathbf{f}\right) - \nabla\cdot\boldsymbol{\sigma} = 0 \quad \text{on } \Omega_t \times (0,T), \tag{1}$$

$$\nabla\cdot\mathbf{u} = 0 \quad \text{on } \Omega_t \times (0,T). \tag{2}$$

Here ρ, $\mathbf{u}$, $\mathbf{f}$, and $\boldsymbol{\sigma}$ are the density, velocity, body force, and the stress tensor, respectively. The stress tensor consists of its isotropic and deviatoric parts,

$$\boldsymbol{\sigma} = -p\mathbf{I} + \mathbf{T}, \quad \mathbf{T} = 2\mu\boldsymbol{\varepsilon}(\mathbf{u}), \quad \boldsymbol{\varepsilon}(\mathbf{u}) = \frac{1}{2}((\nabla\mathbf{u}) + (\nabla\mathbf{u})^T), \tag{3}$$

where p, $\mathbf{I}$ and μ are the pressure, identity tensor, and dynamic viscosity, respectively. Let $(\Gamma_t)_g$ and $(\Gamma_t)_h$ be the subsets of the boundary, Γ_t, on which the Dirichlet and Neumann-type boundary conditions are specified, respectively. The boundary conditions are employed as follows:

$$\mathbf{u} = \mathbf{g} \; on \; (\Gamma_t)_g, \quad \mathsf{n}\cdot\boldsymbol{\sigma} = \mathbf{h} \; on \; (\Gamma_t)_h, \tag{4}$$

where n is the unit vector normal to the boundary.

The initial condition on the velocity is applied on Ω_t at $t = 0$,

$$\mathbf{u}(\mathbf{x}, 0) = \mathbf{u}_0 \quad on \; \Omega_t, \tag{5}$$

where $\mathbf{u}_0$ is divergence free.

Pressure and viscous stresses around the surface of the cylinder are integrated for calculating the force coefficient, $\mathbf{C_x}$. The lift coefficient (C_l) is normal to the freestream direction, and the drag coefficient (C_d) is along the freestream. $\mathbf{C_x}$ is given as

$$\mathbf{C_x} = \frac{1}{\frac{1}{2}\rho U_\infty^2 D}\int_{\Gamma_{cyl}} \boldsymbol{\sigma}\,\hat{\mathsf{n}}\,d\Gamma \tag{6}$$

where $\hat{\mathsf{n}}$ is the unit vector that is normal to the cylinder boundary, Γ_{cyl} and $\mathbf{C_x}$ represents $\hat{i}C_d + \hat{j}C_l$.

B. Equations of motion for a rigid body

The oscillatory motion of the rigid body, caused by the unsteady fluid forces exerted on its surface, is governed by the following equations:

$$m\ddot{x} + c\dot{x} + kx = F_x, \tag{7}$$

$$m\ddot{y} + c\dot{y} + ky = F_y. \tag{8}$$

Here $\ddot{x}$, $\dot{x}$, and x are the acceleration, velocity, and displacements of the cylinder, respectively, along the x-axis, whereas $\ddot{y}$, $\dot{y}$, and y represent the same quantities in the y-direction. F_x and F_y are the horizontal and vertical components of the fluid force acting on the body. m, k, and c are mass of the cylinder, spring constant, and damping coefficient, respectively.

Let the nondimensional parameters be defined as follows: $\ddot{Y} = \ddot{y}D/U_\infty^2$, $\dot{Y} = \dot{y}/U_\infty$, $Y = y/D$, and $\xi = c/c_c$, where critical damping (c_c) is $2\sqrt{km}$. Substituting these nondimensional parameters, m^* and F_N, which are defined in Sec. I, and C_d and C_l [defined in Eq. (6)] in Eqs. 7 and 8, the following nondimensional equations are obtained:

$$\ddot{X} + 4\pi F_N\zeta\dot{X} + (2\pi F_N)^2 X = \frac{2C_d}{\pi m^*} \quad \text{for (0,T)}, \tag{9}$$

$$\ddot{Y} + 4\pi F_N\zeta\dot{Y} + (2\pi F_N)^2 Y = \frac{2C_l}{\pi m^*} \quad \text{for (0,T)}, \tag{10}$$

C. The finite element formulation

This section presents the stabilized space-time finite element formulation, employed to solve the flow-governing equations on a moving domain. Here, the time interval $(0, T)$ is divided into subintervals $I_n = (t_n, t_{n+1})$, where t_n and t_{n+1} belong to a series of time levels in $(0, T)$. Assume Q_n is the space-time slab that consists of a spatial subdomain Ω_n and its boundary surface P_n, where P_n is formed by the trace of Γ_n in the time interval I_n. Dirichlet and Neumann type boundary conditions are specified on $(P_n)_g$ and $(P_n)_h$, respectively, which are the two parts of P_n. For each space-time slab, we define the trial function spaces $(\mathcal{S}^h_{\mathbf{u}})_n$ and $(\mathcal{S}^h_p)_n$ respectively, for velocity and pressure, and the same for weighting function spaces are $(\mathcal{V}^h_{\mathbf{u}})_n$ and $(\mathcal{V}^h_p)_n$, as provided by Tezduyar *et al.*,[31,32] and are shown below:

$$(\mathcal{S}^h_{\mathbf{u}})_n = \{\mathbf{u}^h | \mathbf{u}^h \in [H^{1h}(Q_n)]^{n_{sd}}, \mathbf{u}^h = \mathbf{g}^h \quad \text{on } (P_n)_g\}, \tag{11}$$

$$(\mathcal{V}^h_{\mathbf{u}})_n = \{\mathbf{w}^h | \mathbf{w}^h \in [H^{1h}(Q_n)]^{n_{sd}}, \mathbf{w}^h = 0 \quad \text{on } (P_n)_g\}, \tag{12}$$

$$(\mathcal{S}^h_p)_n = (\mathcal{V}^h_p)_n = \{p^h | p^h \in H^{1h}(Q_n)\}. \tag{13}$$

Here $H^{1h}(Q_n)$ represents the finite dimensional function space over the space-time slab Q_n.

The stabilized finite element formulation of the flow equations is written as follows: given $(\mathbf{u}^h)_{n-}$, find $\mathbf{u}^h \in (\mathcal{S}^h_{\mathbf{u}})_n$ and $p^h \in (\mathcal{S}^h_p)_n$ such that $\forall \mathbf{w}^h \in (\mathcal{V}^h_{\mathbf{u}})_n$, $q^h \in (\mathcal{V}^h_p)_n$,

$$\begin{aligned}
&\int_{Q_n} \mathbf{w}^h \cdot \rho \left(\frac{\partial \mathbf{u}^h}{\partial t} + \mathbf{u}^h \cdot \nabla \mathbf{u}^h - \mathbf{f} \right) dQ \\
&\quad + \int_{Q_n} \boldsymbol{\varepsilon}(\mathbf{w}^h) : \boldsymbol{\sigma}(p^h, \mathbf{u}^h) dQ + \int_{Q_n} q^h \nabla \cdot \mathbf{u}^h dQ \\
&\quad + \sum_{e=1}^{n_{el}} \int_{Q^e_n} \frac{1}{\rho} \tau \left[\rho \left(\frac{\partial \mathbf{w}^h}{\partial t} + \mathbf{u}^h \cdot \nabla \mathbf{w}^h \right) - \nabla \cdot \boldsymbol{\sigma}(q^h, \mathbf{w}^h) \right] \\
&\quad \cdot \left[\rho \left(\frac{\partial \mathbf{u}^h}{\partial t} + \mathbf{u}^h \cdot \nabla \mathbf{u}^h - \mathbf{f} \right) - \nabla \cdot \boldsymbol{\sigma}(p^h, \mathbf{u}^h) \right] dQ \\
&\quad + \sum_{e=1}^{n_{el}} \int_{Q^e_n} \delta \nabla \cdot \mathbf{w}^h \rho \nabla \cdot \mathbf{u}^h dQ + \int_{\Omega_n} (\mathbf{w}^h)^+_n \cdot \rho \left((\mathbf{u}^h)^+_n \right. \\
&\quad \left. - (\mathbf{u}^h)^-_n \right) d\Omega = \int_{(P_n)_h} \mathbf{w}^h \cdot \mathbf{h}^h dP.
\end{aligned} \tag{14}$$

In the discrete equation given in (14), the following notations are used:

$$(\mathbf{u}^h)^{\pm}_n = \lim_{\epsilon \to 0} \mathbf{u}(t_n \pm \epsilon), \tag{15}$$

$$\int_{Q_n} (\dots) \, dQ = \int_{I_n} \int_{\Omega_n} (\dots) \, d\Omega \, dt, \tag{16}$$

$$\int_{P_n} (\dots) \, dP = \int_{I_n} \int_{\Gamma_n} (\dots) \, d\Gamma \, dt, \tag{17}$$

$$(\mathbf{u}^h)^-_0 = \mathbf{u}_0. \tag{18}$$

In the formulation provided in (14), the first three integrals are Galerkin terms, whereas the fourth and fifth terms are added to provide stability to the solution. Sixth one is the jump term, which loosely connects the solution on either side of each space-time slab. More details about the physical meaning of the terms and stability parameters, τ and δ, can be found in the articles reported by Tezduyar *et al.*[31–33] The linear algebraic equation system resulting from the finite element discretization of the governing equations are solved iteratively by employing the Generalized Minimal Residual (GMRES) procedure[34] in conjunction with diagonal pre-conditioners. For each nonlinear iteration in solving the flow governing equations, mesh is updated to the new coordinates by solving the equations of linear elasticity, as proposed by Johnson and Tezduyar.[35]

III. FINITE ELEMENT MESH AND COMPUTATIONAL DETAILS

Figure 1 shows the finite element mesh over full domain and the close-up view of the three staggered cylinders. Here onwards, the upstream cylinder is referred to as cyl-A, and the two downstream bodies are referred to as cyl-B and cyl-C [see Fig. 1(b)]. All the cylinders are of equal diameter (D). The gap in the streamwise (x-) direction between the upstream and downstream cylinders is $5D$. The two downstream bodies are placed symmetrically on either side of cyl-A with a vertical distance of $3D$ between them. The center of cyl-A is located at (0, 0) [see Fig. 1(b)]. In Fig. 1(a), L_U and L_D represent the distances to upstream and downstream boundaries of the domain, respectively, from the center, while H is the height of the domain. The mesh consists of a structured part around the cylinders, which is adequately refined to capture the boundary layer. The rest of the domain is made of an unstructured mesh created via Delaunay's triangulation technique.

A. Boundary conditions

Boundary conditions, employed in the computational domain, are shown in Fig. 1(a). On the upstream boundary, velocity (U_∞) of the uniform flow in the x-direction is specified. This boundary condition directs the flow to enter the domain with a uniform velocity in the x-direction, while the component of velocity along the y-axis is zero. On the downstream boundary, gradients of velocity across the end wall are considered zero, which physically means that it is a stress-free boundary. Symmetry conditions are employed on the top and bottom walls, on which the normal component of velocity and tangential stress are set to zero values. This boundary condition implies that the fluid can slip along the walls but cannot penetrate them. No slip condition is provided on the cylinders' surfaces, which indicates that both the components of flow velocity are zero. However, as the cylinder moves, its velocity components in the x- and y-directions are updated on the surface of the body for every nonlinear iteration.

B. Mesh convergence study

In order to study the effect of mesh refinement and the dimensions of the domain on the flow characteristics, three meshes (referred to as M1, M2, and M3) are employed in the computation of $Re = 150$ case. The number of nodes and elements of all the meshes are presented in the caption of Table I, which shows the values of various parameters obtained by each mesh. For M1 and M2, $L_U = 8D$, $L_D = 50D$, and $H = 25D$, while for M3, $L_U = 16D$, $L_D = 80D$, and $H = 25D$. Note that H

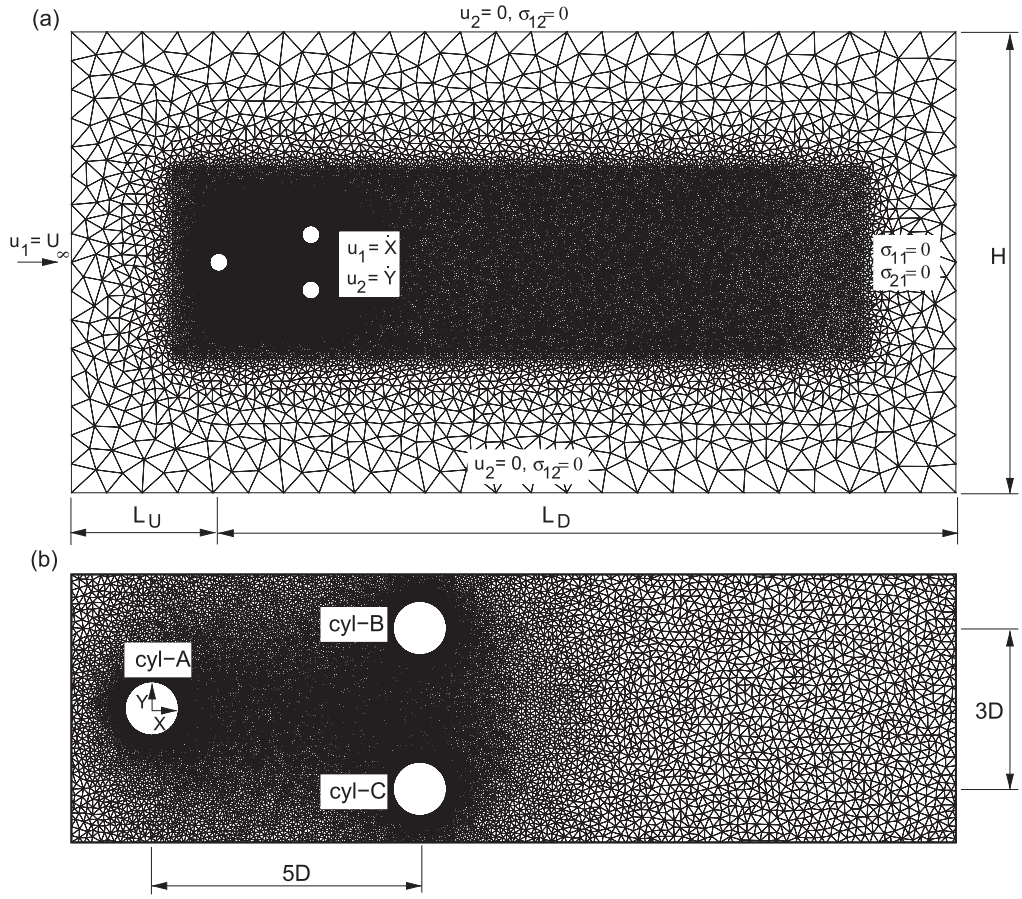

FIG. 1. (a) Finite element mesh over full domain and (b) close-up view of the cylinders.

is kept the same for all the three meshes, as it is demonstrated by Prasanth *et al.*[36] and Prasanth and Mittal[26] that the height of the domain significantly affects the dynamic response of the freely oscillating cylinder. The number of nodes of the three meshes (see the caption of Table I) suggest that M2 is over 1.8 times larger than M1, while M3 provides the same resolution as that of M1. From Table I, it can be observed that the mean transverse amplitude ($A_{y,mean}$), mean drag coefficient ($\overline{C_d}$), *rms* values of the lift coefficient ($C_{l,rms}$) as well as the ratio of vibration frequency (f_v), and the natural frequency (f_N) of the spring-mass system predicted by all the three meshes are in good agreement. This study confirms that mesh-M1 is adequate for the range of *Re* considered in the present work. Therefore, M1 is employed for all the simulations. Effect of the time step (Δt) is also investigated, providing $\Delta t = 0.01$ and 0.05. We observed that the difference in the solution is less than 1%, and hence, $\Delta t = 0.05$ is considered.

TABLE I. Vortex-induced vibrations of three staggered cylinders ($Re = 150$, $m^* = 10$ and $\xi = 0$): Comparison of the nondimensional mean amplitude ($A^*_{y,mean}$) of transverse oscillations, average drag coefficient ($\overline{C_d}$), *rms* value of lift coefficient ($C_{l,rms}$), and frequency ratio (f_v/f_N) obtained for three meshes. Number of nodes and elements of M1: 39 804, 79 290; M2: 73 504, 146 592; M3: 44 031, 88 744.

Mesh	cyl	$A^*_{y,mean}$	$\overline{C_d}$	$C_{l,rms}$	f_v/f_N
M1	cyl-1	4.257×10^{-2}	1.184	0.322	1.596
M2	cyl-1	4.237×10^{-2}	1.179	0.320	1.625
M3	cyl-1	4.304×10^{-2}	1.181	0.313	1.597
M1	cyl-2	0.276	1.245	0.777	1.028
M2	cyl-2	0.275	1.235	0.767	1.020
M3	cyl-2	0.276	1.244	0.762	1.025
M1	cyl-3	0.279	1.251	0.779	1.028
M2	cyl-3	0.271	1.241	0.777	1.020
M3	cyl-3	0.281	1.225	0.761	1.025

C. Computational details

All the simulations are performed on a distributed memory computing machine, which is loaded with MPI (Message Passing Interface) libraries and Intel compilers. Dynamic mesh partitioning is carried out employing ParMETIS.[37] More details of the parallel algorithm, employed in the present implementation, are provided by Behara and Mittal.[38] Computation for each time step that consists of three nonlinear iterations in solving the fluid dynamic equations, and five iterations of mesh moving equations for a nonlinear iteration, takes approximately 11 s on a 12 processor computing machine.

IV. OSCILLATION RESPONSE OF CYLINDERS

Figure 2(a) shows the variation of normalized maximum amplitude (A^*_y) of the transverse oscillations with *Re* for all the three cylinders. In the present simulations, it is observed that for certain *Re*, the two downstream cylinders exhibit nonperiodic oscillations at various amplitudes. Due to this fact, we surmise that plotting the mean amplitude provides a better insight

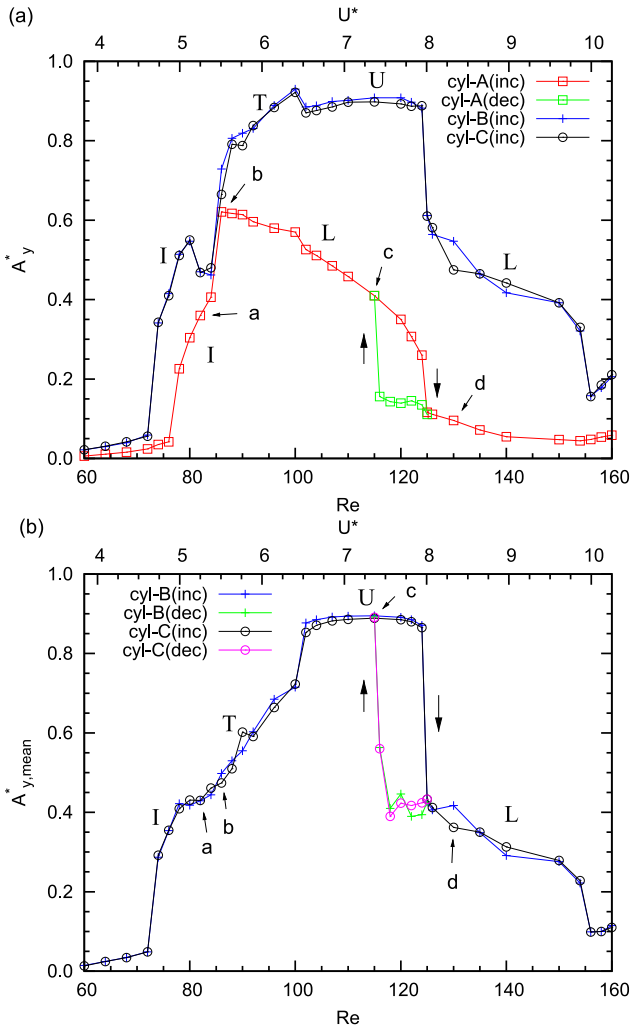

FIG. 2. (a) Variation of normalized maximum transverse amplitude (A^*_y) for all three cylinders and (b) variation of normalized mean transverse amplitude ($A^*_{y,mean}$) for the downstream cylinders with increasing (inc) and decreasing (dec) Re. Letters I, T, U, and L represent the initial lock-in branch, transition region, and upper and lower lock-in branches, respectively. Letters a to d point out the Reynolds numbers for which time histories of y/D and flow pictures are shown in Figs. 4 and 5, respectively. Upward and downward arrows indicate the hysteresis.

into the oscillation response. Therefore, the variation of normalized mean amplitude ($A^*_{y,mean}$) with Re for the two downstream cylinders (cyl-B and cyl-C) is presented in Fig. 2(b). Here, $A^*_{y,mean}$ is calculated by averaging the magnitudes of amplitudes, on either side of the mean position of the cylinder, over all the oscillation cycles considered. The corresponding values of reduced velocity (U^*) are shown on the top axis of each plot.

From Fig. 2(a), one can observe that cyl-A exhibits initial (I) and lower (L) synchronization response branches. This lock-in behavior is the same as that observed by Prasanth and Mittal[26] for an isolated cylinder at low Reynolds numbers. This phenomenon confirms that the oscillation response of the upstream cylinder is not affected by the presence of downstream cylinders, since vortex shedding takes place in the gap between the upstream and downstream bodies. cyl-B and cyl-C exhibit the upper branch (U) as well, in addition to the initial (I) and lower (L) branches. These three amplitude response branches can clearly be seen on both A^*_y—and $A^*_{y,mean}$—Re plots in Fig. 2. The oscillation response of downstream cylinders undergoes gradual transition from the initial to the upper branch. This transition region is denoted by "T" in Fig. 2. On the other hand, in the upper ⇒ lower mode transition, a sudden downward jump occurs in the maximum and mean amplitudes. This jump is associated with hysteresis, as shown in Fig. 2(b). To the best of our knowledge, all the above-mentioned aspects, with respect to the behavior of oscillating downstream cylinders, are observed for the first time. Interestingly, these phenomena are similar to the dynamic response of a transversely vibrating isolated cylinder[22,27] at higher Re [$\sim O(10^4)$]. Therefore, in the rest of this paper, various vibration responses of the downstream bodies are compared with the isolated cylinder's behavior, reported by Khalak and Williamson.[22]

Figure 3 shows the ratio of vibration frequency (f_v) of the cylinder and the natural frequency (f_N) of the spring-mass system as well as the Strouhal frequency (St) in the wake of the oscillating cylinder, plotted as functions of Re. As the cylinders exhibit non-synchronized oscillations for $Re \leq 76$, they vibrate at a frequency, which is nearly equal to the frequency (f) of primary vortex shedding in the wake of stationary cylinders. Therefore, f_v/f_N closely follows the diagonal solid line that represents f/f_N in Fig. 3(a). From Fig. 2, one can observe that for cyl-B and cyl-C, the initial lock-in branch begins at a lower Reynolds number than the corresponding Re of cyl-A. Therefore, the upward jump occurs in f_v/f_N at $Re = 74$ for the downstream cylinders and at $Re = 78$ for cyl-A, as shown in the inset of Fig. 3(a). In the initial branch, all the cylinders exhibit nearly periodic oscillations. Figure 4 shows the time histories of normalized transverse displacements (y/D) of cyl-A and cyl-C for the values of Re, which are marked by the letters "a" to "d" in Fig. 2. In this figure, data related to cyl-B are not shown since cyl-B's oscillation response is almost the same as that of cyl-C. From the time histories of y/D at $Re = 82$ in Fig. 4(a), it is evident that the cylinders exhibit nearly periodic oscillations in the initial branch.

Even though the initial branch begins at different Re for the upstream cylinder and the two downstream bodies, it ends at $Re = 84$ for all the three cylinders. In the case of cyl-A, the lower branch begins immediately at $Re = 86$, whereas the initial branch is followed by the transition to the upper response mode for the downstream bodies (cyl-B and cyl-C), as shown in Fig. 2. Therefore, at $Re = 86$, cyl-A undergoes periodic oscillations corresponding to its lower mode, while cyl-C exhibits beats-like phenomenon [see Fig. 4(b)]. The transition regime ends at $Re = 100$, while both the downstream cylinders achieve the upper response branch for $102 \leq Re \leq 124$. This upper mode is characterized by a periodic oscillation response, as is evident from Fig. 4(c). These aspects are in contrast with the observations of Khalak and Williamson.[22] They reported that for an isolated cylinder that oscillates in the transverse direction only, there is a sudden jump in the amplitude response from initial to the upper mode and the upper branch is associated with nonperiodic oscillations.

The oscillation response of the downstream cylinders jumps from the upper to the lower mode at $Re = 125$. At the same Re, cyl-A's vibration response goes out of the lock-in regime and jumps to the desynchronization region. For cyl-B

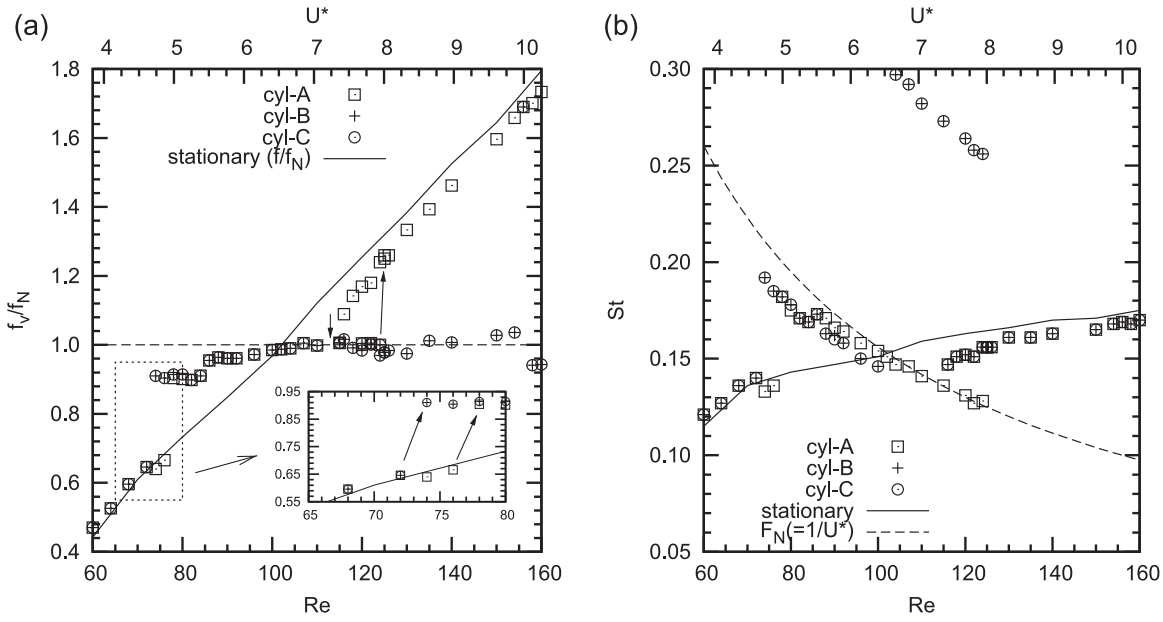

FIG. 3. (a) Variation of ratio of vibration frequency (f_v) and natural frequency (f_N) and (b) variation of Strouhal frequency (St) in the wake of vibrating cylinders, with respect to Re. In (a), the diagonal solid line represents the ratio of primary shedding frequency (f) in the wake of stationary cylinders and f_N. In (b), the dashed line represents nondimensional natural frequency (F_N) of the spring-mass system.

and cyl-C, the lower lock-in mode appears during $125 \leq Re \leq 154$ (see Fig. 2). In the lower branch, the downstream cylinders experience nonperiodic vibrations, as can be noticed from the y/D history of cyl-C at $Re = 130$ in Fig. 4(d). Contrary to this observation, Khalak and Williamson[22] demonstrated that the lower branch of an isolated cylinder is marked by a periodic oscillation response. Figure 4(d) shows that since cyl-A exhibits desynchronized oscillations at $Re = 130$, it exhibits oscillations at low amplitudes.

Figure 3(a) shows that f_v/f_N for cyl-B and cyl-C appears close to the $f_v/f_N = 1$ line for all the three lock-in modes. Whereas in the case of cyl-A, since its vibration response

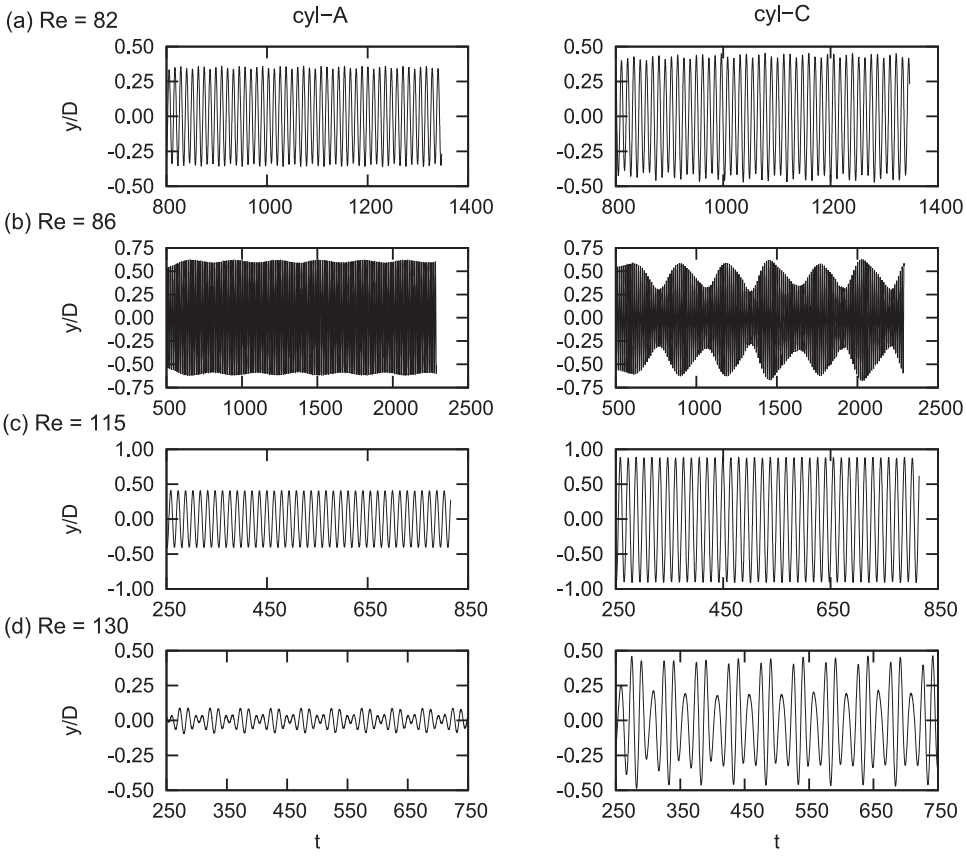

FIG. 4. Time histories of normalized transverse displacement (y/D) at the Re, which are pointed by the letters (a)–(d) in Fig. 2.

reaches the desynchronization regime for $Re \geq 125$, f_v/f_N departs from the unity and closely follows the f/f_N line. These aspects indicate that for $Re \geq 125$, the upstream cylinder exhibits desynchronized oscillations at primary shedding frequency (f) corresponding to the stationary cylinders, while the downstream bodies vibrate at natural frequency (f_N) of the spring-mass system. The lower lock-in regime (L) for cyl-B and cyl-C continue up to $Re = 154$, and at $Re = 156$, their oscillation responses jump to the desynchronization regime, as shown in Fig. 2.

V. PRIMARY VORTEX SHEDDING

Figure 5 presents the instantaneous vorticity pictures for the values of Re, which are marked by the letters "a" to "d" in Fig. 2, while the corresponding Strouhal frequency (St) spectra for cyl-C are shown in Fig. 6. Since the cylinders exhibit nearly periodic oscillations at $Re = 82$ (see Fig. 4), which is in the initial branch, the 2S mode of vortices are shed at regular intervals by all bodies, as can be seen in Fig. 5(a). This aspect results in a single peak appearing in the St spectrum at $Re = 82$ (see Fig. 6). As the oscillation response of the downstream cylinders transitions from the initial to the upper response mode, vortex shedding undergoes low frequency modulation. Therefore, St spectrum at $Re = 86$ is characterized by two peaks, f_1 and f_2, as shown in Fig. 6. Figure 5(b) shows that at $Re = 86$, in the wake of each downstream cylinder, the vortices are organized in two rows. From this figure, it can also be observed that the 2S mode of shedding occurs in the transition regime as well. With the vibration response of the downstream bodies achieving an upper response mode, which is associated with the periodic oscillations, the shedding becomes periodic as seen in Fig. 5(c). As a result, the single peak appears at $Re = 115$ in Fig. 6. However, interestingly, it is observed that in the upper branch, downstream cylinders shed the P+S mode of vortices. This phenomenon will be discussed in detail later. In the lower branch, the wake is characterized by the 2S shedding pattern. In this lower mode, since cyl-B and cyl-C exhibit nonperiodic oscillations [see Fig. 4(d)], the vortices appear randomly shed in the wake as shown in Fig. 5(d).

Figure 3(b) shows that in the nonsynchronization region for $Re < 74$, all the three oscillating cylinders shed vortices at a frequency, nearly equal to the Strouhal frequency of stationary cylinders. For the oscillating upstream cylinder (cyl-A), St closely follows the reduced natural frequency (F_N) of the spring-mass system in initial and lower branches (for $78 \leq Re \leq 124$), as seen in Fig. 3(b). On the other hand, the

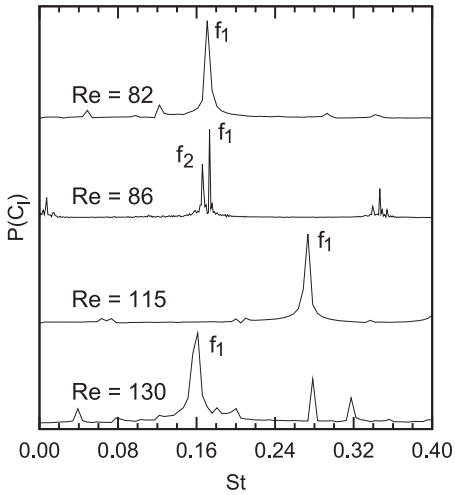

FIG. 6. Strouhal frequency (St) spectra for a downstream cylinder that is referred to as cyl-C in Fig. 1, at the Re, which are pointed by letters a to d, in Fig. 2.

vibrating downstream cylinders shed primary vortices nearly at the natural frequency (F_N), only in the initial excitation and transition regions (for $72 < Re < 102$). However, during the upper response regime (for $102 \leq Re \leq 124$), primary shedding takes place at $St > 0.25$ in the wakes of cyl-B and cyl-C. The peak-f_1 in the frequency spectrum of $Re = 115$ (see Fig. 6) also confirms that St is significantly high in the upper branch. We observed that this high Strouhal frequency is associated with the P+S mode of shedding by the downstream cylinders. As cyl-A's oscillation response goes out of the synchronization regime and cyl-B and cyl-C exhibit lower mode for $Re > 125$, Strouhal frequencies become nearly equal to the primary shedding frequency of the stationary system, as shown in Fig. 3(b).

Figure 7 shows one cycle of normalized transverse displacement (y/D) of cyl-C at $Re = 115$, which is in the upper branch, and for the corresponding time period, the variation of the lift coefficient (C_l) is also presented. As one can notice from this figure, for one cycle of y/D, C_l exhibits slightly more than 1.5 cycles. On the C_l–t curve, letters a to e mark nearly the crests and troughs using solid circles, while the corresponding y/D locations of cyl-C are indicated by the letters a′ to e′. Figure 8 presents vorticity pictures in the near wake at the time instants corresponding to points a to d marked on the y/D–t curve in Fig. 7. Since the flow pattern related to point "a" repeats at "e," the flow picture for "e" is not shown. Figure 9 presents the pictures of the pressure field at the same time instants, as marked by the letters "a" to "d" in Fig. 7.

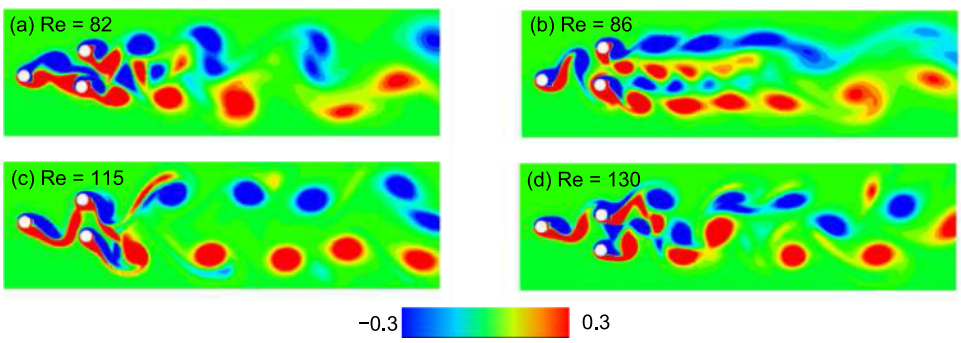

FIG. 5. Instantaneous vorticity field at the Re, which are pointed by the letters (a)–(d) in Fig. 2.

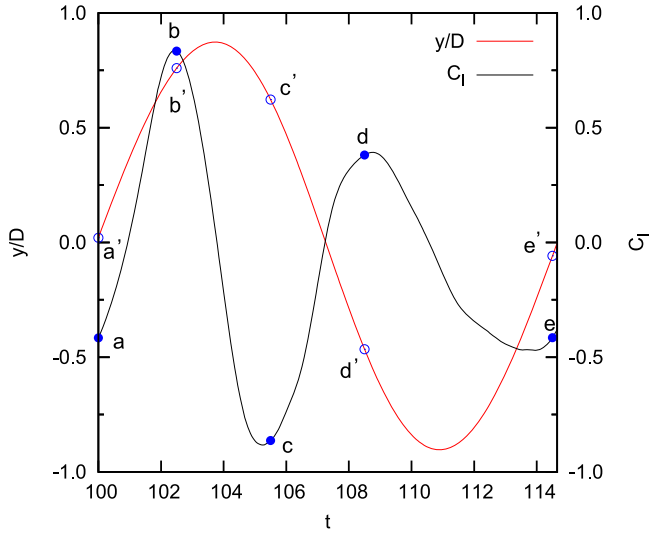

FIG. 7. One cycle of time history of normalized transverse displacement (y/D) of cyl-C and the history of the lift coefficient (C_l) exerted on the same cylinder and for the same time period. Letters a to e and the corresponding solid circles indicate nearly the crests and troughs of C_l curve, while the letters a′ to e′ and the open circles indicate the corresponding transverse location (y/D) of the body.

Figures 7–9 illustrate the physical aspects associated with the appearance of 1.5 cycles of C_l for one oscillation cycle in the transverse direction. From Fig. 8(a), it can be observed that at $t = 100$, the vortices shed by cyl-A are at far upstream to cyl-C. Therefore, the effect of those vortices on cyl-C is not significant. At this time instant, cyl-C is moving upwards, as is evident from its y/D location indicated by a′ in Fig. 7. The lift, exerted on the body due to its upward motion, acts downwards. Also, the stagnation point is found on the upper half of the cyl-C's surface [see Fig. 9(a)]. As a result, the body experiences slightly negative lift (point a in Fig. 7). At point b′ in Fig. 7, cyl-C decelerates as it is approaching the peak of y/D–t curve. At the same time, the negative vortex on the upper shoulder becomes stronger [see Fig. 8(b)], leading to the formation of higher suction in the upper half, as shown in Fig. 9(b). Therefore, net pressure force acts on the body upwards, resulting in positive C_l (see point b in Fig. 7). Figure 8(c) shows that the positive vortex, shed by cyl-A, interacts with the boundary layer and free shear layers on cyl-C. This interaction reduces the intensity of negative vorticity on the upper shoulder of cyl-C, while augmenting the positive vortex on the cylinder's lower surface. This phenomenon creates higher suction on the lower side of cyl-C, as can be seen in Fig. 9(c). Therefore, lift acts downwards on the body (see point c in Fig. 7). At point d′ in Fig. 7, cyl-C is moving downwards and the negative vortex, shed by cyl-A interacts with the negative vortex forming on the upper side of cyl-C [see Fig. 8(d)], causing the net pressure force acting upwards on the body. Therefore, lift is positive at point d in Fig. 7. At point e, the flow pattern resembles the one shown in Fig. 8(a).

In the present simulations, it is observed that the interaction with vortices shed from the upstream cylinder significantly affects the timing of vortex shedding by the downstream bodies, leading to the formation of the P+S mode in the near wake. One can clearly see this phenomenon in the flow pictures, presented in Fig. 8. Figure 8(a) shows that in the vicinity of cyl-B, one pair of positive and negative vortices is shed and has moved a little downstream, while a positive vortex is being released from its bottom shoulder. From Fig. 8(b), it is evident that the pair of vortices shed by cyl-B moved further downstream, and the positive vortex released from its lower side coalesced with that of cyl-C, thus increasing the intensity of positive vortex shed by cyl-C. This completes the process of P+S vortex shedding in a cycle. Similar phenomena can be observed for cyl-C

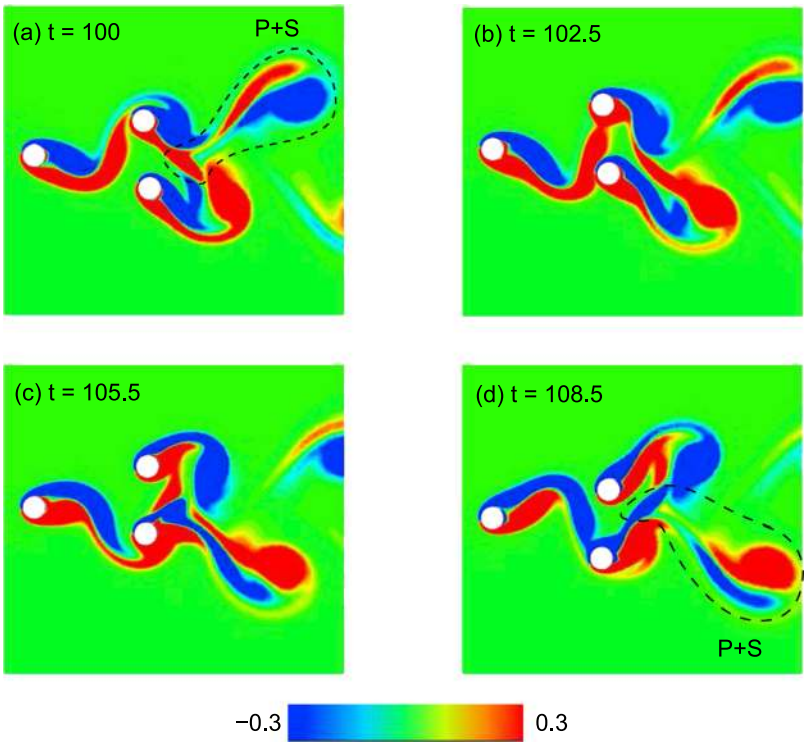

FIG. 8. Instantaneous vorticity field in the near wake of the cylinders for the time instants, which are pointed by letters a to d in Fig. 7. The flow pattern at point e is not shown, since it is the same as that of (a). Loops of dashed lines in figures (a) and (d) highlight the P+S mode of vortex shedding.

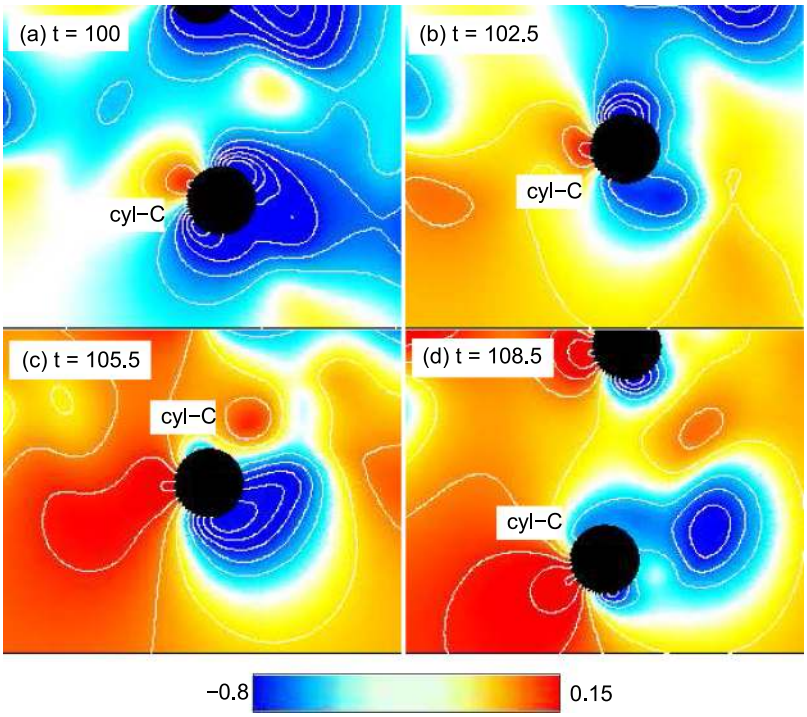

FIG. 9. Pressure field around cyl-C at the time instants, pointed by letters (a)–(d) in Fig. 7.

as well. Figures 8(a)–8(c) depict the formation and shedding of one pair of vortices in the near wake of cyl-C, while in Fig. 8(d), one can notice that the negative vortex is about to separate from the body and merge with the negative vortex of cyl-B, completing the formation of the P+S mode. To the best of our knowledge, this is for the first time that the P+S mode

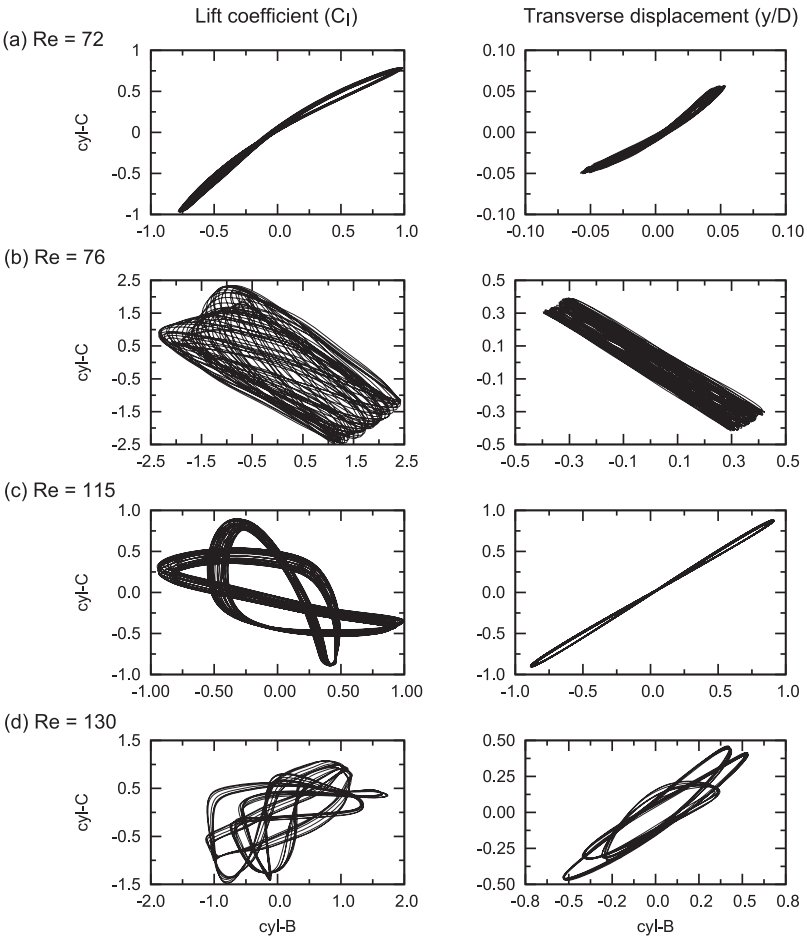

FIG. 10. Phase between the lift (C_l) as well as traverse displacement (y/D) of the two downstream cylinders at various *Re*.

is observed during the synchronization regime at such low *Re* in the wake of a freely oscillating cylinder, either in the case of an isolated cylinder or for multiple cylinders. From Fig. 8, it is evident that the positive vortex released by cyl-B and the negative vortex shed from cyl-C are weaker than their counterparts and get diffused as they move downstream. Therefore, the pattern of the far downstream wake appears to be of the 2S mode, as can be seen in Fig. 5(c). It can be argued that the P+S shedding leads to the appearance of 1.5 cycles in the history of C_l per one cycle of body's transverse displacement (see Fig. 7).

VI. PHASE BETWEEN THE TRANSVERSE MOTION OF DOWNSTREAM CYLINDERS

Figure 10 presents the phase relation between cyl-B and cyl-C for lift (C_l) as well as the transverse motion (y/D) at various *Re*. At the beginning of the initial excitation mode, lift acting on both the downstream cylinders is in phase with each other as shown in Fig. 10(a). Therefore, their respective transverse movements also exhibit the same phase. However, with an increase in *Re* towards the end of the initial mode, interestingly, both C_l and y/D of the downstream cylinders go out of phase by 180°, as can be seen in Fig. 10(b). Figures 10(c) and 10(d) indicate that that in the upper and lower modes, even as the phase relation of C_l exhibits certain random behavior, the transverse displacement of cyl-B is in phase with the corresponding y/D of cyl-C.

VII. PHASE BETWEEN LIFT AND TRANSVERSE DISPLACEMENT

Figure 11 shows the $\{C_l{:}y/D\}$ phase plots for cyl-A and cyl-C at various *Re*. Since the phase plots for cyl-B appear similar to those of cyl-C, they are not presented in Fig. 11. From this figure, one can observe that at *Re* = 82, which is in the initial response mode, the transverse motion for all the bodies is in phase with the lift. From Fig. 11(b), it is evident that in the lower branch corresponding to cyl-A, C_l is significantly low; however, the $\{C_l{:}y/D\}$ phase plot suggests that C_l undergoes nearly two cycles of variation for each oscillation cycle of the body. Notwithstanding the existence of 2:1 ratio in the $\{C_l{:}y/D\}$ plot, only the 2S mode of vortices is found in the near wake of cyl-A. On the other hand, the downstream cylinders experience the lift of considerable magnitudes at *Re* = 115, which corresponds to the upper branch, as can be seen in Fig. 11(b). Since nearly 1.5 cycles of C_l appear for one cycle of y/D (see Fig. 7) at *Re* = 115, the $\{C_l{:}y/D\}$ phase plot assumes the shape of figure "8." However, the average phase, computed for both cyl-A and cyl-C, get close to zero value. Figures 11(c) and 11(d) show that cyl-A, in the later part of its lower branch as well as in the desynchronization regime, experiences the phase of nearly 180°. Whereas for the downstream cylinders, the average phase, computed from the $\{C_l{:}y/D\}$ phase plot shown in Fig. 11(c), results in zero value. This aspect suggests that in the lower branch, the transverse vibrations of cyl-B and cyl-C are in phase with the lift. The $\{C_l{:}y/D\}$ phase plot of cyl-C in Fig. 11(d) reveals

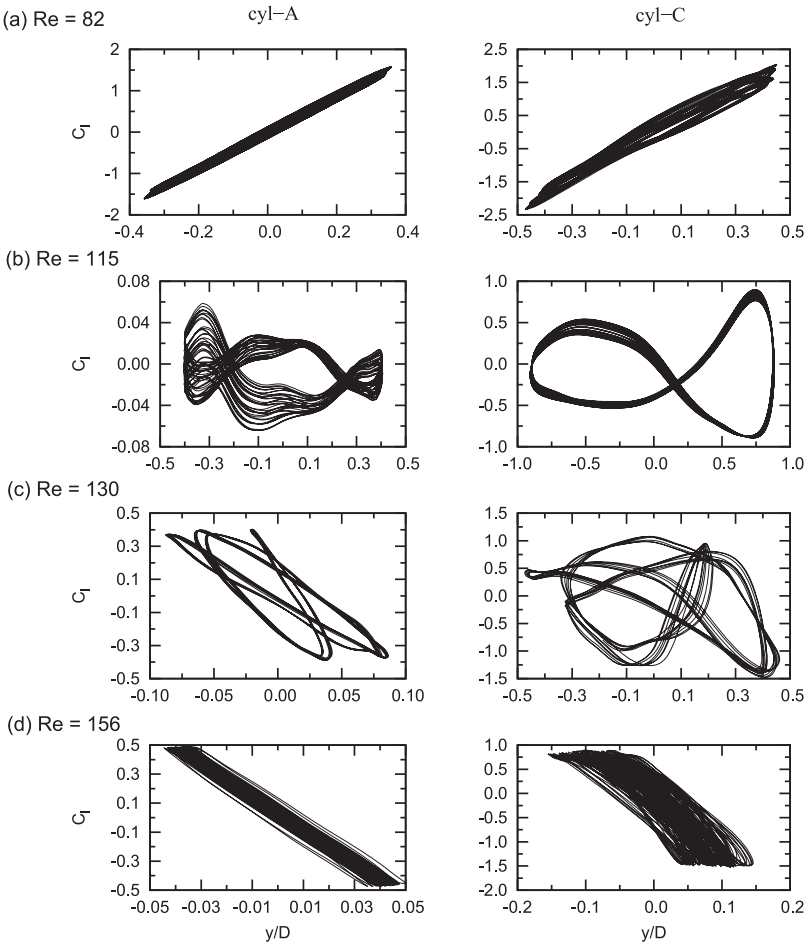

FIG. 11. $\{C_l{:}y/D\}$ phase plots at various *Re*.

that at $Re = 156$, which is in the desynchronization regime, the phase difference becomes 180°.

The phase (ϕ) between the lift and transverse displacement is calculated employing Gilbert transform. Figure 12 presents the variation of ϕ with Re, for cyl-A and cyl-C. On these plots, variation of $A^*_{y,mean}$ is also shown for reference. From Fig. 12(a), it can be observed that for cyl-A, the phase jumps from 0° to nearly 180° in the middle of the lower branch. However, this jump in phase does not affect the vortex shedding pattern, as cyl-A sheds only the 2S mode of vortices for all the Re considered. Prasanth and Mittal[26] also observed the 180° phase jump for an isolated cylinder at certain Re in the lower lock-in branch. They observed that this phase jump is associated with the frequency ratio (f_v/f_N) attaining the value of 1. On the other hand, the downstream cylinders exhibit oscillations, in phase with C_l, for all the three synchronization regimes. From Fig. 12(b), one can notice that the phase jumps to 180° at Re = 156, where the oscillation response jumps from the lower branch to the desynchronization region. This phase jump does not influence the shedding pattern in the wake of downstream cylinders, as the 2S mode is observed in the lower response branch as well as in the desynchronization regime.

VIII. STREAMWISE AMPLITUDE RESPONSE

Variation of the normalized maximum amplitude (A^*_x) of streamwise oscillations with Re is shown in Fig. 13 for all the cylinders. The upstream cylinder (cyl-A) exhibits oscillations predominantly in the transverse direction similar to an isolated body. From Fig. 13, it is evident that cyl-A exhibits a low amplitude response, while the downstream cylinders undergo oscillations at significant amplitudes in the streamwise direction. As one can notice from Fig. 13, for cyl-B and cyl-C, the amplitude increases to $A^*_x \sim 0.2$ in the initial lock-in branch (indicated by I in Fig. 13) and varies around that value in

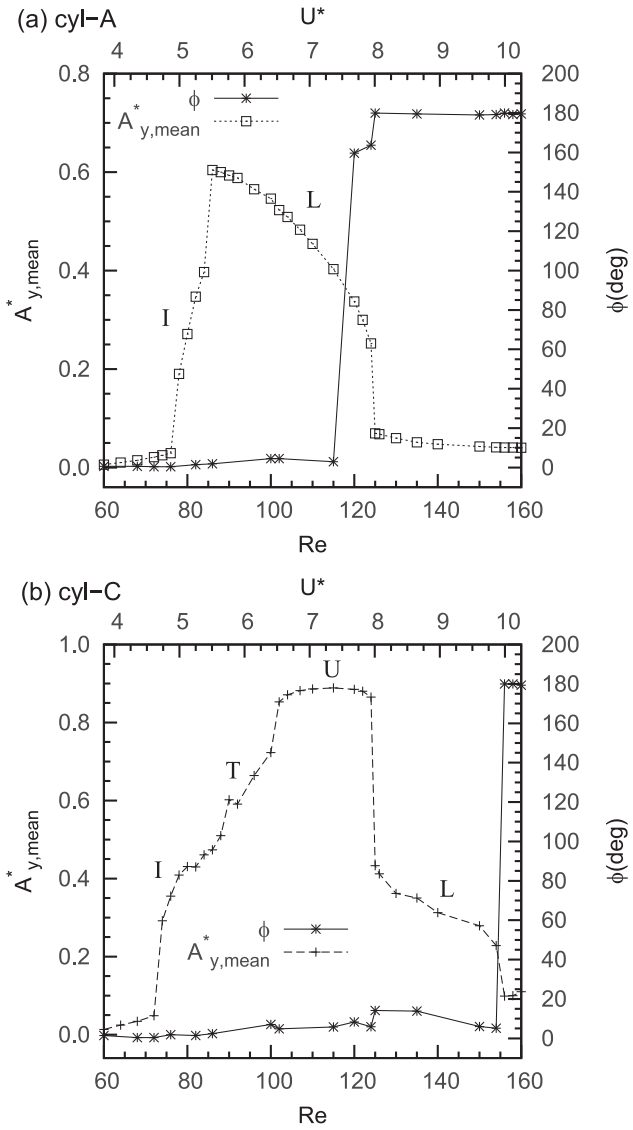

FIG. 12. Variation of the phase (ϕ) between lift exerted on a cylinder and its transverse displacement with Re. Variation of $A^*_{y,mean}$ is also shown for reference. Meanings of letters I, T, U, and L are provided in the caption of Fig. 2.

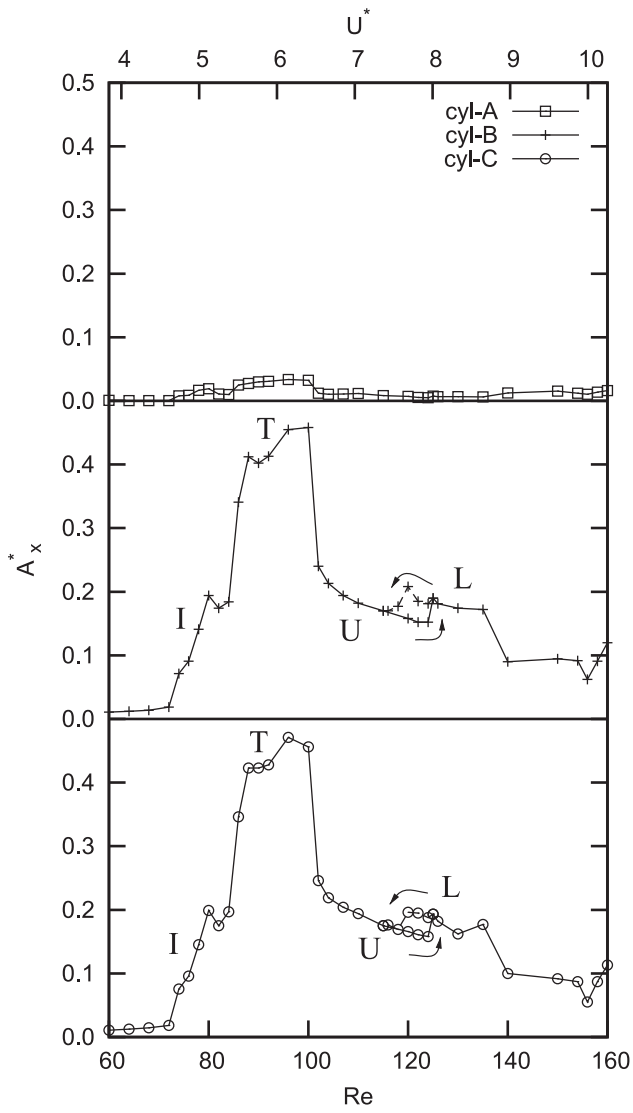

FIG. 13. Variation of normalized maximum amplitude (A^*_x) of streamwise oscillations with Re. Arrows indicate hysteresis. Meanings of letters I, T, U, and L are provided in the caption of Fig. 2.

the upper (U) and lower (L) synchronization regions as well. However, in the transition (T) from the initial to the upper response mode, A_x^* exhibits large values, as cyl-B and cyl-C oscillate at higher amplitudes in the streamwise direction. Note that in Fig. 13, only maximum amplitude is plotted. We shall present details of the cylinder trajectories on the *xy*-plane in Sec. X.

IX. FORCE COEFFICIENTS

Figure 14 shows the variation of *rms* values of C_d and C_l with *Re* for all the three cylinders. In this figure, it can be observed that for cyl-A, the trends in the $C_{d,rms}$–*Re* and $C_{l,rms}$–*Re* relations are similar to those reported for an isolated cylinder by Prasanth and Mittal.[26] This aspect further confirms that the dynamic response of cyl-A is the same as that of a single cylinder for the streamwise gap of 5*D* between the upstream and downstream bodies, considered in the present simulations. However, cyl-B and cyl-C exhibit different phenomena in the $C_{d,rms}$–*Re* and $C_{l,rms}$–*Re* plots compared with cyl-A. In Fig. 14(a), one can observe that for the downstream cylinders, $C_{d,rms}$ rises to its maximum value at the end of the initial branch (I) and jumps to a lower value as transition to the upper response mode begins. In the transition region (T), $C_{d,rms}$ attains another peak, while in the upper branch (U), it decreases monotonically. Whereas, throughout the lower branch (L), $C_{d,rms}$ exhibits negligible variation, as can be seen in Fig. 14(a). In this figure, hysteresis is seen at the transition from the upper to lower branch. On the other hand, Fig. 14(b) shows that the variation of $C_{l,rms}$ for cyl-B and cyl-C is similar to that of cyl-A in their initial (I) and lower (L) branches. However, in the lower branch of cyl-A, $C_{l,rms}$ monotonically decreases, while for the downstream cylinders, this trend is intercepted by the transition region (T), as shown in Fig. 14(b). Hysteresis in the upper ⇒ lower transition can be observed in the $C_{l,rms}$-*Re* plot as well.

X. TRAJECTORIES OF CYLINDERS

Recall that the amplitudes of streamwise oscillations of cyl-A are negligible compared with those of cyl-B and cyl-C, for all the *Re* considered (see Fig. 13). Therefore, cyl-A oscillates predominantly in the transverse direction. Whereas, for the downstream cylinders it is interesting to see the trajectories on the *xy*-plane, since both the bodies exhibit streamwise oscillations at significant amplitudes. Trajectories of cyl-C are shown in Fig. 15 for various *Re*. In this figure, trajectories of cyl-B are not presented, as they are similar to those of cyl-C. Note that in all the plots of *xy*-displacement, scale on the *x*-axis is magnified. Figure 15(a) shows that at *Re* = 72, which is in the nonsynchronization region, the downstream cylinder vibrates along an oval-like path. However, the amplitudes in both *x*- and *y*-directions are negligible. In the initial and upper branches, the downstream cylinders traverse along elliptical orbits, which are oriented in opposite directions, as shown in Figs. 15(b) and 15(e), respectively. In Sec. V, it is observed that in the initial branch, cyl-B and cyl-C shed the 2S mode of vortices, while the upper branch is associated with the P+S pattern of vortex shedding. Also, it is shown that the P+S shedding leads to the appearance of 1.5 cycles of C_l for each cycle of *y*/*D* (see Fig. 7) in the upper branch. However, this P+S shedding does not alter the shape of trajectory of the downstream cylinders. From Figs. 15(c) and 15(d), it can be observed that in the transition regime, cyl-C moves along several elliptical trajectories, which are of various sizes and are oriented in different directions. Also from these figures, it is interesting to notice that as *Re* increases in the transition regime, the orientation of the elliptical trajectory gradually shifts from its orientation corresponding to the initial branch [see Fig. 15(b)] to the orientation observed in the upper branch [Fig. 15(e)]. Figure 15(f) shows that in the lower branch, the downstream cylinders oscillate along a certain closed path periodically. We observed that with an increase in *Re* in the lower response mode, this periodicity ceases to exist, as cyl-B and cyl-C oscillate randomly on the *xy*-plane.

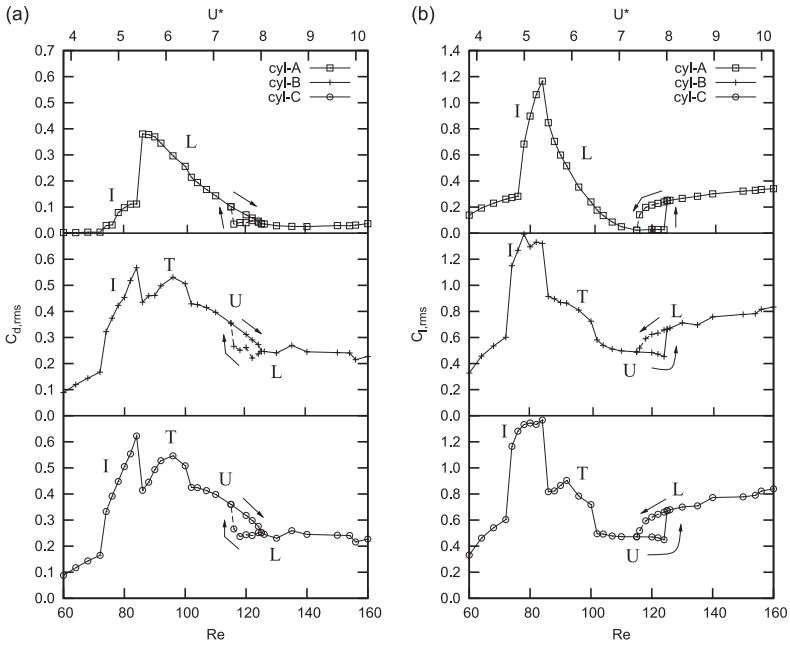

FIG. 14. Variation of (a) $C_{d,rms}$ and (b) $C_{l,rms}$ with *Re*. Arrows indicate hysteresis. Meanings of letters I, T, U, and L are provided in the caption of Fig. 2.

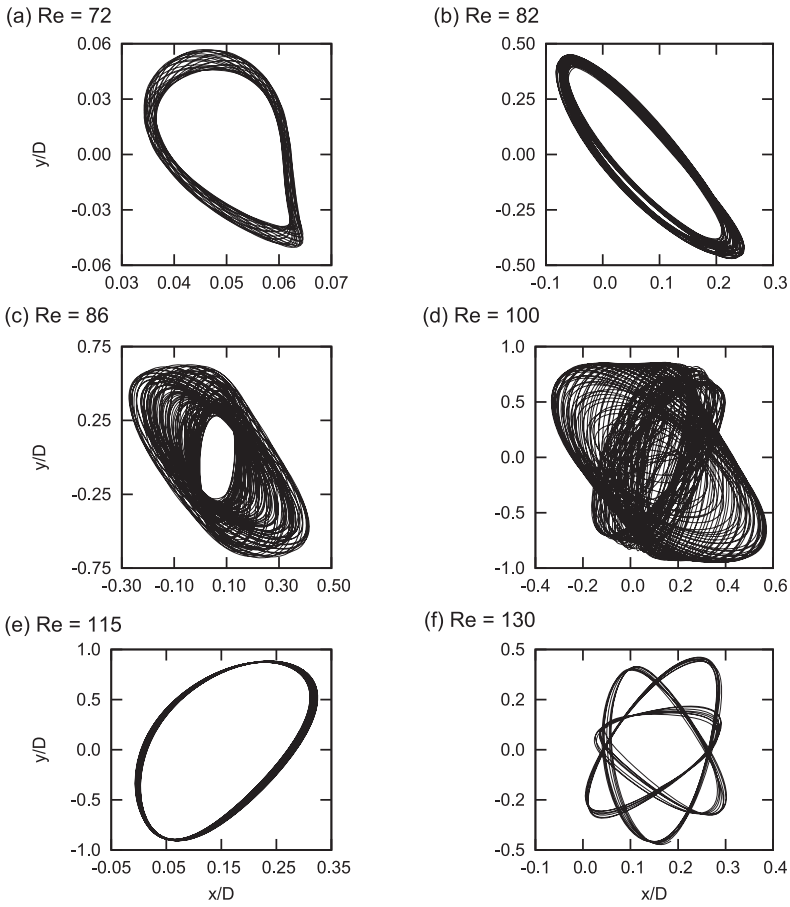

FIG. 15. Trajectories of cyl-C at various *Re*.

XI. CONCLUSIONS

Vortex-induced vibrations of three circular cylinders, arranged in staggered configuration, are studied via two-dimensional finite element computations for Reynolds numbers in the range of Re = 60–160. Identical cylinders are mounted on elastic supports in both x- and y-directions, with the streamwise distance between the upstream and downstream bodies being $5D$. Since the two downstream cylinders are placed symmetrically on either side of the horizontal (x-) axis of the domain, with a transverse gap of $3D$ between them, both the bodies exhibit nearly the same dynamic response.

It is observed that the upstream cylinder exhibits the initial and lower lock-in regimes, similar to the dynamic response of an isolated cylinder, reported by Prasanth and Mittal[26] for low Re. This phenomenon confirms that for the streamwise gap of $5D$, between the upstream and downstream cylinders, the upstream body is not affected by the presence of downstream bodies. Whereas the oscillation response of both the downstream cylinders achieve the upper lock-in mode in addition to the initial and the lower modes. To the best of our knowledge, these distinct synchronization modes corresponding to a downstream cylinder are observed for the first time. The initial excitation regime of the upstream cylinder is immediately followed by its lower lock-in mode. However, in the case of downstream cylinders, the dynamic response undergoes gradual transition from the initial to the upper mode. On the other hand, a downward jump takes place in the amplitude as the oscillation response shifts from the upper to lower branch. This jump is associated with hysteresis. The upper branch is characterized by periodic oscillations of the downstream cylinders, while in the lower branch oscillations are nonperiodic. Exactly opposite phenomena are observed by Khalak and Williamson[22] for an isolated cylinder, with respect to the oscillation response in the upper and the lower modes.

The upstream cylinder sheds the 2S mode of vortices for all Re considered. The downstream bodies also shed the 2S mode except for the upper branch. In the upper branch corresponding to the downstream cylinders, it is observed that their interaction with the vortices shed by the upstream body as well as high transverse amplitudes (where, $A_y^* \sim 0.9D$) changes the timing of vortex shedding. As a result, the downstream cylinders shed the P+S mode of vortices. This P+S mode is associated with the appearance of high Strouhal frequency in the upper branch.

In the case of the upstream cylinder, a 180° phase jump occurs at certain Re corresponding to its lower branch, in consistence with observation of Prasanth and Mittal[26] for an isolated body. Whereas for the downstream cylinders, the phase difference between the lift and the transverse displacement appears close to zero value throughout the synchronization regime and jumps to 180° as the oscillation response shifts from the lower mode to the desynchronization region.

[1]M. M. Zdravkovich, "Review of flow interference between two circular cylinders in various arrangements," ASME J. Fluids Eng. **99**, 618 (1977).
[2]M. M. Zdravkovich, "Review of interference-induced oscillations in flow past two parallel circular cylinders in various arrangements," J. Wind Eng. Ind. Aerodyn. **28**, 183 (1988).
[3]S. S. Chen, "A review of flow-induced vibration of two circular cylinders in crossflow," ASME J. Pressure Vessel Technol. **108**, 382 (1986).

[4]D. Sumner, "Two circular cylinder in cross-flow: A review," J. Fluids Struct. **26**, 849–899 (2010).
[5]C. H. K. Williamson and R. Govardhan, "Vortex induced vibrations," Annu. Rev. Fluid Mech. **36**, 413 (2004).
[6]A. Bokaian and F. Geoola, "Wake-induced galloping of two interfering circular cylinders," J. Fluid Mech. **146**, 383 (1984).
[7]D. Brika and A. Laneville, "The flow interaction between a stationary cylinder and a downstream flexible cylinder," J. Fluids Struct. **13**, 579 (1999).
[8]F. S. Hover and M. S. Triantafyllou, "Galloping response of a cylinder with upstream wake interference," J. Fluids Struct. **15**, 503 (2001).
[9]G. R. S. Assi, J. R. Meneghini, J. A. P. Aranha, P. W. Bearman, and E. Casaprima, "Experimental investigation of flow-induced vibration interference between two circular cylinders," J. Fluids Struct. **22**(6), 819 (2006).
[10]G. V. Papaioannou, D. K. P. Yue, M. S. Triantafyllou, and G. E. Karniadakis, "On the effect of spacing on the vortex-induced vibrations of two tandem cylinders," J. Fluids Struct. **24**, 833 (2008).
[11]T. K. Prasanth and S. Mittal, "Vortex-induced vibration of two circular cylinders at low Reynolds number," J. Fluids Struct. **25**, 731–741 (2009).
[12]I. Borazjani and F. Sotiropoulos, "Vortex-induced vibrations of two cylinders in tandem arrangement in the proximity–wake interference region," J. Fluid Mech. **621**, 321–364 (2009).
[13]P. W. Bearman, "Circular cylinder wakes and vortex-induced vibrations," J. Fluids Struct. **27**, 648–658 (2011).
[14]B. S. Carmo, S. J. Sherwin, P. W. Bearman, and R. H. J. Willden, "Flow-induced vibration of a circular cylinder subjected to wake interference at low Reynolds number," J. Fluids Struct. **27**, 503–522 (2011).
[15]F. J. Huera-Huarte and P. W. Bearman, "Vortex and wake-induced vibrations of a tandem arrangement of two flexible circular cylinders with near wake interference," J. Fluids Struct. **27**, 193–211 (2011).
[16]F. J. Huera-Huarte and M. Gharib, "Vortex- and wake-induced vibrations of a tandem arrangement of two flexible circular cylinders with far wake interference," J. Fluids Struct. **27**, 824–828 (2011).
[17]G. R. S. Assi, "Wake-induced vibration of tandem cylinders of different diameters," J. Fluids Struct. **50**, 329–339 (2014).
[18]G. R. S. Assi, "Wake-induced vibration of tandem and staggered cylinders with two degrees of freedom," J. Fluids Struct. **50**, 340–357 (2014).
[19]H. Wang, W. Yang, K. D. Nguyen, and G. Yu, "Wake-induced vibrations of an elastically mounted cylinder located downstream of a stationary larger cylinder at low Reynolds numbers," J. Fluids Struct. **50**, 479–496 (2014).
[20]Z. Han, D. Zhou, and J. Tu, "Wake-induced vibrations of circular cylinder behind a stationary square cylinder using a semi-implicit characteristic-based split scheme," J. Eng. Mech. **140**(8), 04014059 (2014).
[21]R. C. Mysa, A. Kaboudian, and R. K. Jaiman, "On the origin of wake-induced vibration in two tandem circular cylinders at low Reynolds number," J. Fluids Struct. **61**, 76–98 (2016).
[22]A. Khalak and C. H. K. Williamson, "Motions, forces and mode transitions in vortex-induced vibrations at low mass-damping," J. Fluids Struct. **13**, 813 (1999).
[23]G. R. S. Assi, P. W. Bearman, and J. R. Meneghini, "On the wake-induced vibration of tandem circular cylinders: The vortex interaction excitation mechanism," J. Fluid Mech. **661**, 365–401 (2010).
[24]S. Mittal and V. Kumar, "Flow-induced oscillations of two cylinders in tandem and staggered arrangements," J. Fluids Struct. **15**, 717 (2001).
[25]D. Brika and A. Laneville, "Vortex-induced vibrations of a long flexible circular cylinder," J. Fluid Mech. **250**, 481 (1993).
[26]T. K. Prasanth and S. Mittal, "Vortex-induced vibrations of a circular cylinder at low Reynolds numbers," J. Fluid Mech. **594**, 463 (2008).
[27]R. Govardhan and C. H. K. Williamson, "Modes of vortex formation and frequency response of a freely vibrating cylinder," J. Fluid Mech. **420**, 85 (2000).
[28]C. H. K. Williamson and A. Roshko, "Vortex formation in the wake of an oscillating cylinder," J. Fluids Struct. **2**, 355 (1988).
[29]H. Blackburn and R. Henderson, "Lock-in behaviour in simulated vortex-induced vibration," Exp. Therm. Fluid Sci. **12**, 184 (1996).
[30]S. P. Singh and S. Mittal, "Vortex-induced oscillations at low Reynolds numbers: Hysteresis and vortex shedding modes," J. Fluids Struct. **20**, 1085 (2005).
[31]T. E. Tezduyar, M. Behr, and J. Liou, "A new strategy for finite element computations involving moving boundaries and interfaces—The deforming-spatial-domain/space-time procedure: I. The concept and the preliminary numerical tests," Comput. Methods Appl. Mech. Eng. **94**, 339 (1992).
[32]T. E. Tezduyar, M. Behr, S. Mittal, and J. Liou, "A new strategy for finite element computations involving moving boundaries and interfaces—The deforming-spatial-domain/space-time procedure: II. Computations of free-surface flows, two liquid flows, and flows with drifting cylinders," Comput. Methods Appl. Mech. Eng. **94**, 353 (1992).
[33]T. E. Tezduyar, S. Mittal, S. E. Ray, and R. Shih, "Incompressible flow computations with stabilized bilinear and linear equal order interpolation velocity pressure elements," Comput. Methods Appl. Mech. Eng. **95**, 221 (1992).
[34]Y. Saad and M. Schultz, "GMRES: A generalized minimal residual algorithm for solving nonsymmetric linear systems," SIAM J. Sci. Stat. Comput. **7**, 856 (1986).
[35]A. A. Johnson and T. E. Tezduyar, "Mesh update strategies in finite element computations of flow problems with moving boundaries and interfaces," Comput. Methods Appl. Mech. Eng. **119**, 73 (1994).
[36]T. K. Prasanth, S. Behara, S. P. Singh, R. Kumar, and S. Mittal, "Effect of blockage on vortex-induced vibrations at low Reynolds numbers," J. Fluids Struct. **22**, 865 (2006).
[37]G. Karypis, ParMETIS–Parallel Graph Partitioning and Fill-reducing Matrix Ordering, 2013, URL: http://glaros.dtc.umn.edu/gkhome/metis/parmetis/overview.
[38]S. Behara and S. Mittal, "Parallel finite element computation of incompressible flows," Parallel Comput. **35**, 195 (2009).